Research Square

Preprints are preliminary reports that have not undergone peer review.
They should not be considered conclusive, used to inform clinical practice,
or referenced by the media as validated information.

The Effect of Dwell Time on Al/Ti Refill Friction Stir Spot Welded Joints: Diffusion Behavior and Mechanical Properties

Jiancheng Wang
Harbin Institute of Technology Weihai
Li Zhou
Harbin Institute of Technology
Xinchen Nan
Harbin Institute of Technology Weihai
Chengyue Ma
Harbin Institute of Technology Weihai
Shikang Gao
hitAkang@163.com
Harbin Institute of Technology Weihai https://orcid.org/0000-0003-1288-3130
Yuchun Liu
Harbin Institute of Technology Weihai
Xiaoguo Song
Harbin Institute of Technology Weihai

Research Article

Keywords: Refill friction stir spot welding, Dwell time, Al/Ti dissimilar metals, Microstructure, Mechanical properties

Posted Date: August 4th, 2026

DOI: https://doi.org/10.21203/rs.3.rs-10513159/v1

License: This work is licensed under a Creative Commons Attribution 4.0 International License.
Read Full License

The Effect of Dwell Time on Al/Ti Refill Friction Stir Spot Welded Joints: Diffusion Behavior and Mechanical Properties

Jiancheng Wang[1,2], Li Zhou[1,2*], Xinchen Nan[1,2], Chengyue Ma[2], Shikang Gao[1,2*], Yuchun Liu[1,2], Xiaoguo Song[1,2]

[1] *State Key Laboratory of Precision Welding & Joining of Materials and Structures, Harbin Institute of Technology, Harbin, 150001, People's Republic of China*

[2] *Shandong Provincial Key Laboratory of Special Welding Technology, Harbin Institute of Technology at Weihai, Weihai 264209, People's Republic of China*

Corresponding author: Shikang Gao, E-mail: hitAkang@163.com

Li Zhou, E-mail: zhou.li@hit.edu.cn

Abstract:

With the rapid development of the aerospace industry, Al/Ti has received widespread attention as a dissimilar material with excellent properties. Refill friction stir spot welding (RFSSW) has been proven to offer distinct advantages in joining dissimilar materials. However, the interfacial diffusion behavior and mechanical properties of Al/Ti dissimilar material joints remain unclear. This study investigates interfacial metallurgical bonding in Al/Ti joints via RFSSW with varying dwell times, using a combined numerical simulation and experiment. The results indicate that with a prolonged dwell time, both the peak temperature and strain rate increased, resulting in grain coarsening and a thicker diffusion layer in the joint. In agreement with its low Gibbs free energy and interfacial energy, $TiAl_3$ is identified as the sole intermetallic compound at the interface via transmission electron microscopy. The tensile-shear failure load initially increases and then decreases, reaching a maximum of 6.39 kN at a dwell time of 6 s. This trend is attributed to the presence of coarse grain zone and hard Ti/$TiAl_3$ particles within the Al plate, which promote crack initiation and propagation.

Keywords: Refill friction stir spot welding; Dwell time; Al/Ti dissimilar metals; Microstructure; Mechanical properties

1 Introduction

The rapid advancement of aerospace and related fields has led to increased research on Al/Ti dissimilar materials, owing to their high strength-to-weight ratio and superior high-temperature resistance[1,2]. However, brittle intermetallic compounds (IMCs) tend to form in Al-Ti weld joints during high-temperature welding, primarily due to crystallographic dissimilarity and significant differences in the thermal conductivity of the two metals. The presence of thicker or discrete IMCs at the Al/Ti interface is due to unstable heat input in the fusion welding process[3]. Common IMCs, such as $TiAl_3$ and TiAl, deteriorate the mechanical properties through crack initiation and propagation mechanisms[4].

Friction stir welding (FSW), as a solid-state joining process, enables metallurgical bonding via severe plastic deformation while maintaining materials in the solid phase. This characteristic effectively eliminates fusion-related defects, including porosity and elemental loss, thereby achieving an effective reduction in the thickness of IMCs[5,6]. Zhou et al.[7] conducted FSW on Al/Ti dissimilar joints and found $TiAl_3$ in the Al/Ti mixture, but no significant IMC layer was observed at the interface. Zhang et al.[8] found an IMC layer at the interface of the Al/Ti friction stir lap welded joint, and the layer thickness increased with increasing rotational speed and decreased with increasing forward speed, which was related to the heat-force coupling diffusion coefficient. In addition, $TiAl_3$ was observed on the Al side, and mainly TiAl was observed at the interface. Nevertheless, FSW inherently generates keyhole defects at the termination of welds, which affects the structural integrity. Refill stir friction spot welding (RFSSW) is a new type of solid-state joining technology proposed by the Helmholtz-Zentrum Geesthacht Research Center to address the keyhole defect challenge. The welding process is illustrated in Fig. 1. The mechanical properties of joints fabricated by RFSSW can be improved by avoiding stress concentration and increasing the effective load-bearing area[9-12]. RFSSW has

been extensively validated for similar material joints in current studies, including aluminum alloy, magnesium alloys, pure copper, and metal matrix composites. Meanwhile, for dissimilar joints, the technology has shown promising results for Al/steel, Al/Cu, and dissimilar Al alloys. However, the RFSSW of Al/Ti dissimilar metals remains underexplored. Vacchi et al.[13] focused only on the corrosion behavior analysis of joint interfaces. The formation mechanism of IMCs along the interface in RFSSW has not yet been fully elucidated.

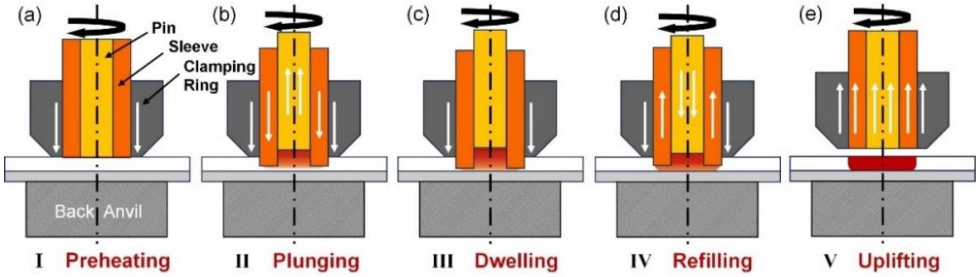


Fig. 1 Schematic of the RFSSW process: (a) preheating stage; (b) plunging stage; (c)dwelling stage; (d) refilling stage; (e) uplifting stage.

The process parameters directly affect the mechanical properties of the joints by affecting the temperature field distribution and strain state. Li et al.[14] revealed that process parameters influenced the texture evolution in RFSSW joints through dynamic recrystallization, and such parameter optimizations can improve the mechanical properties of the joints. In the RFSSW process, the parameters that can be adjusted include plunge depth, rotational speed, dwell time, etc. During welding of low melting-point materials, the tool penetrates into the lower sheet. The plunge depth affects the hook angle and consequently the tensile-shear load of joints. Furthermore, crack propagation paths directly depend on the evolution of the hook geometry[15]. For hard high-melting-point materials, a certain gap is usually maintained between the tool and the lower sheet during plunging to avoid excessive wear[16,17]. An increase in rotational speed significantly elevates joint heat input and accelerates material plastic flow, which in turn modifies the morphology and microstructure of joints[18]. Dwell time, similar to annealing duration, significantly affects the metallurgical bonding mechanism at the Al/Ti interface. Furthermore, RFSSW involves a unique thermo-mechanical effect, yet the effects of dwell time on joint formation have not

been systematically investigated.

To solve these problems, Al/Ti dissimilar joints were produced using RFSSW at different dwell times in this study. The effect of dwell time on the microstructure and mechanical properties of RFSSW joints was analyzed. Additionally, numerical simulations were employed to demonstrate the thermomechanical coupling process of RFSSW. Finally, the IMC formation mechanism and fracture mechanism was investigated.

2 Materials and Methods

In this study, 6061 aluminum alloy with dimensions of 75 mm×30 mm×2 mm and Ti6Al4V titanium alloy with dimensions of 75 mm×30 mm×1.5 mm were selected as the upper and lower plates, respectively. The chemical compositions of the two materials are summarized in Table 1, and the mechanical properties are presented in Table 2.

Table 1 Chemical composition of 6061 aluminum alloy and Ti6Al4V titanium alloy(wt.%)

	Cu	Zn	Mg	Si	Mn	Fe	Al	V	Others	Ti
6061-T6	0.28	0.05	0.9	0.54	0.12	0.10	Bal.	-	-	-
Ti6Al4V	-	-	-	-	-	0.30	6.80	4.50	0.50	Bal.

Table 2 Mechanical properties of the 6061 aluminum alloy and Ti6Al4V titanium alloy.

	Yield strength (MPa)	Ultimate tensile strength (MPa)	Elongation (%)
6061-T6	285	313	10.6%
Ti6Al4V	834	908	13%

The experiment was conducted using a custom-built RFSSW system (Fig. 2a) fabricated with a closed-loop displacement control system and an integrated laser alignment module. The welding tool assembly comprises three critical components machined from the GH4169 nickel-based superalloy: (1) a shoulder sleeve for material plasticization, (2) a threaded probe for material refilling, and (3) a clamping ring to prevent material overflow (Fig. 2b).

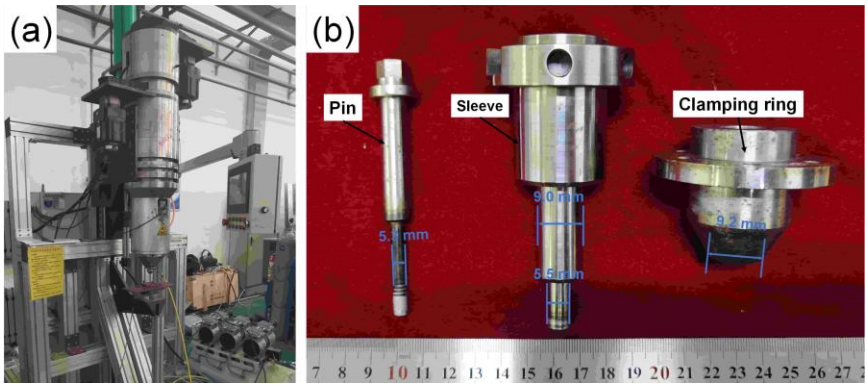


Fig. 2 Equipment and tools: (a) RFSSW equipment; (b) welding tools.

The form of the lap joint is illustrated in Fig. 3, featuring a 30 mm × 30 mm overlap area. The welding area was strategically positioned at the overlap center. Through preliminary experiments, the optimal parameters were identified as a rotational speed of 1300 rpm and a plunge rate of 0.9 mm/s. By maintaining these parameters, dwell times of 2, 4, 6, and 8 s were systematically investigated. To mitigate tool wear and element diffusion risks associated with Ti contact, a plunge depth of 1.8 mm was selected for the welding.

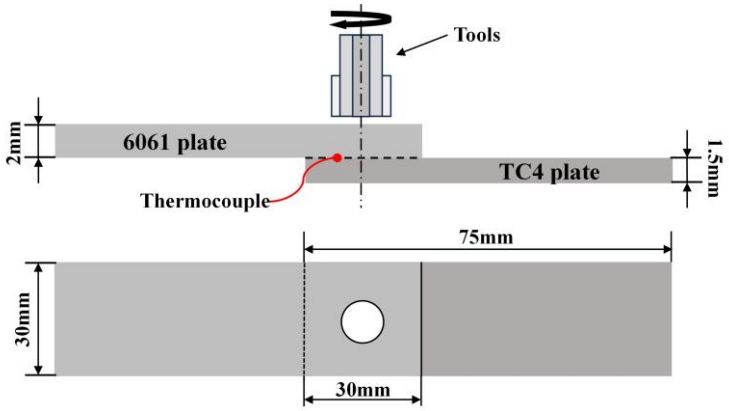


Fig. 3 Schematic of lap joint.

The RFSSW process was numerically simulated and analyzed using a Coupled Eulerian-Lagrangian (CEL) model. To account for severe plastic deformation during RFSSW, the Johnson-Cook (J-C) constitutive model was employed to characterize the coupled thermomechanical material response, as shown in Equation (1). The material parameters of the 6061 aluminum alloy are listed in Table 3[19,20].

$$\sigma_{fs} = \left(\mathrm{A} + \mathrm{B}\bar{\varepsilon}_{pl}^{n}\right)\left(1 + C\ln\frac{\dot{\bar{\varepsilon}}_{pl}}{\dot{\varepsilon}_0}\right)\left[1 - \left(\frac{T - T_{ref}}{T_{melt} - T_{ref}}\right)^{m}\right] \quad (1)$$

Table 3 The material parameters of 6061 aluminum alloy and Ti6Al4V titanium alloy.

	A	B	C	n	m	T_{melt}	T_{ref}
6061	324	114	0.002	0.42	1.34	583 ℃	25 ℃
Ti6Al4V	1098	1092	0.014	0.93	1.1	1630 ℃	25 ℃

The thermal energy generation mechanism of RFSSW comprises two primary components. The first contribution originates from the interfacial friction between the welding tool and workpiece, which can be quantified using Equations (2) and (3). The second contribution arises from the plastic deformation of the material, which is calculated through Equation (4):

$$q_f = \tau\dot{\gamma} \tag{2}$$

$$\tau = \mu P \tag{3}$$

$$q_{pl} = \eta\sigma_{fs}\dot{\varepsilon}_{pl} \tag{4}$$

Where q_f is the surface heat flux density; $\dot{\gamma}$ is the shear rate; τ is the shear stress; μ is the friction coefficient(assigned as 0.7); P is the interfacial normal pressure; q_{pl} is the volumetric heat flux density; η is the conversion of mechanical energy to thermal energy efficiency(generally assigned as 90%); σ_{fs} is the flow stress; $\dot{\varepsilon}_{pl}$ is the plastic strain rate. The temperature-dependent variations in the thermophysical properties of both 6061 and Ti6Al4V alloys are presented in Fig. 4 (a) and (b), respectively[19,21]. Furthermore, the convective heat transfer coefficient between the surface of the workpiece and the air is set to 30 W/(m^2·℃), and the convective heat transfer coefficient between the lower surface of the workpiece and the back anvil is 1000 W/(m^2·℃)[22].

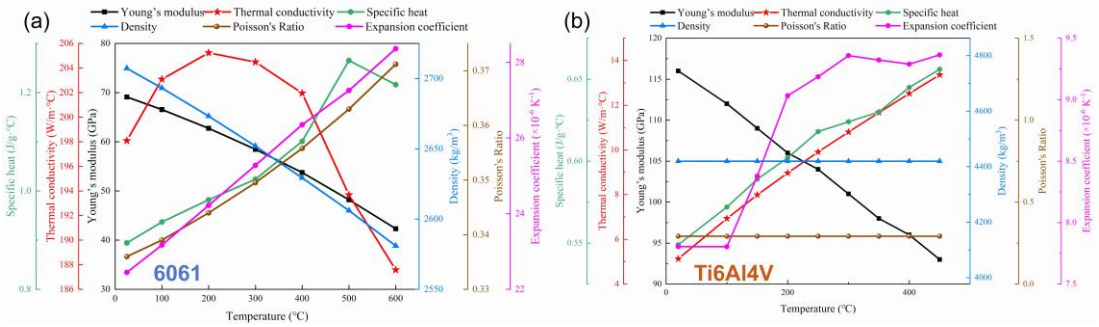


Fig. 4 Temperature-dependent variations in thermophysical properties: (a) 6061; (b) Ti6Al4V.

To balance the computational efficiency with the simulation accuracy, an adaptive mesh refinement strategy was employed, as illustrated in Fig. 5. The weld

zone was divided into 0.5 mm meshes, which progressively coarsened to 4.375 mm meshes in the peripheral regions. The total number of meshes was 33291. By comparing the temperature curve measured by the embedded K-type thermocouples with the simulated temperature curve (see Fig. 5d), it was found that the peak temperature of the experiment reached 393 ℃, while the peak temperature in the simulation was 401 ℃, with a relative error of 2.03%. This indicates that the model can be used to investigate the temperature field evolution and strain distribution of the RFSSW.

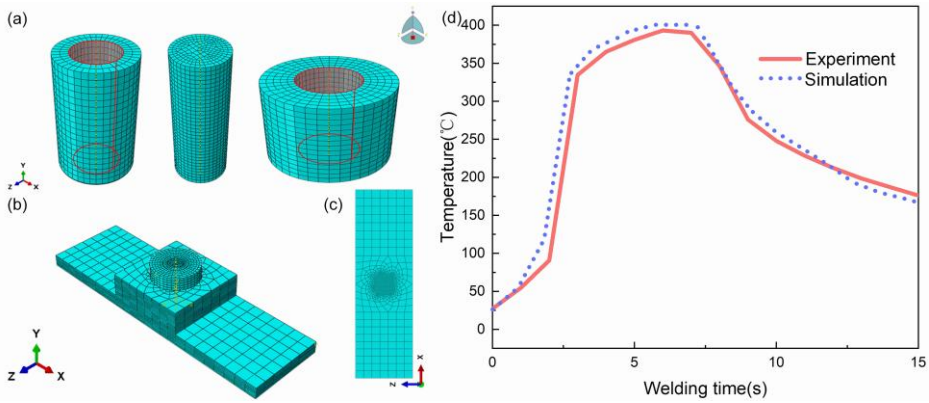


Fig. 5 Simulation models: (a-c) mesh details for tools and substrate; (d) thermal cycling temperature verification.

The metallographic specimens were sectioned using wire electrical discharge machining. Following sequential grinding and polishing, Keller's reagent was used to etch the Al/Ti joints. Microstructural characterization was conducted using optical microscopy (OM) at different dwell times and scanning electron microscopy (SEM) equipped with energy dispersive X-ray spectroscopy (EDS) to determine the thickness and elemental composition of the IMCs. Focused ion beam-prepared (FIB) lamellae from the bonding interface were analyzed using transmission electron microscopy (TEM) at 200 kV. In terms of mechanical properties, a universal testing machine and digital turret microhardness tester were used to measure the tensile-shear properties and hardness, respectively. The thermal cycling temperature of the RFSSW process was monitored using type K thermocouples.

3 Results and Discussion

3.1 Numerical simulation and welding thermal cycle

The dwell time is defined as the duration of concurrent thermal input and mechanical stirring maintained after achieving the target plunge depth[23]. This critical process phase is situated between the plunging and refilling stages, as illustrated in Fig. 6, where the sleeve attains a plunge depth of 1.8 mm. The dwell time is measured from this moment. During the dwelling stage, the sleeve withdrawal creates a transient cavity beneath the upper plate. As the pin subsequently plunges, the material inside the sleeve is immediately compressed downward, refilling the cavity and resulting in a sound weld.

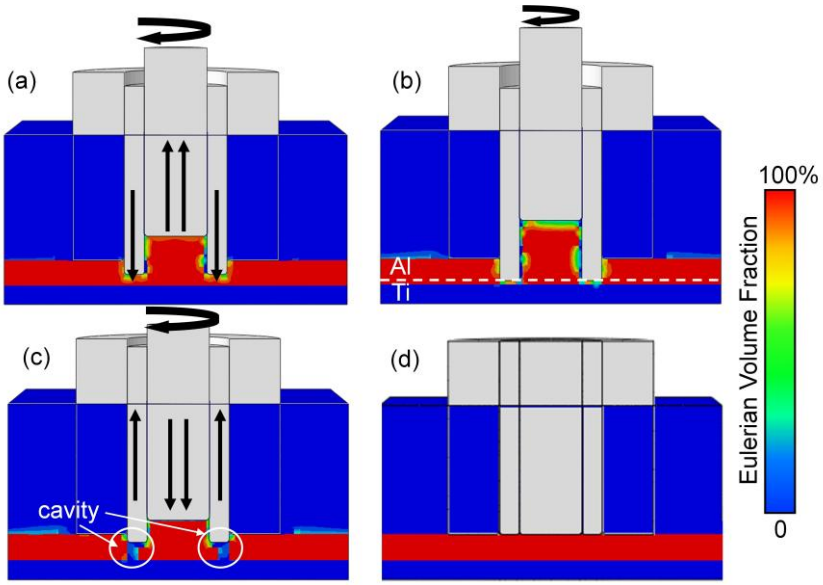


Fig. 6 Simulation results of the RFSSW process: (a) plunging stage; (b) dwelling stage; (c) refilling stage; (d) uplifting stage.

The strain distribution characteristics for varying dwell times were investigated through numerical simulation, as shown in Fig. 7. The equivalent plastic strain maintains axisymmetric along the centerline, and the peak strain is concentrated at the end of the sleeve periphery. This is consistent with the simulation results of Janga[24], indicating that plastic deformation in the sleeve region is most severe during the dwelling stage. Dwell time extension induces strain rate intensification, generating a pronounced asymmetry distribution. The equivalent plastic strain fields demonstrate preferential accumulation peripheral to the advancing side (AS) versus the retreating side (RS). This asymmetric plastic strain along the joint thickness is mainly attributed to thermomechanical effects, specifically, the differential thermal gradients and

material flow conditions across the AS/RS[25].

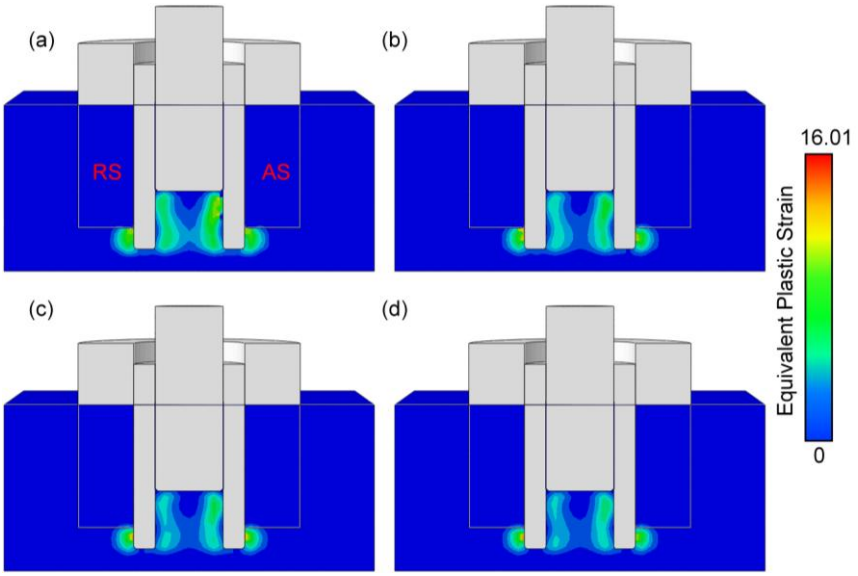


Fig. 7 The strain field distribution: (a) 2 s; (b) 4 s; (c) 6 s; (d) 8 s.

Fig. 8 illustrates temperature field distribution characteristics during RFSSW processes under varying dwell times. The temperature field maintains symmetry along the stirring zone centerline. During the dwelling stage, intense friction between the sleeve and workpiece materials governs heat generation, so the highest temperature is concentrated in the cavity between the sleeve and the pin. The temperature distribution exhibits nonuniformity along sheet thickness, with temperature fields gradually decaying as increasing distance from the sleeve, resulting in a U-shaped isotherm. As dwell time is extended from 2 s to 8 s, the peak temperature increases, driving differential thermal diffusion across the Al/Ti dissimilar joint.

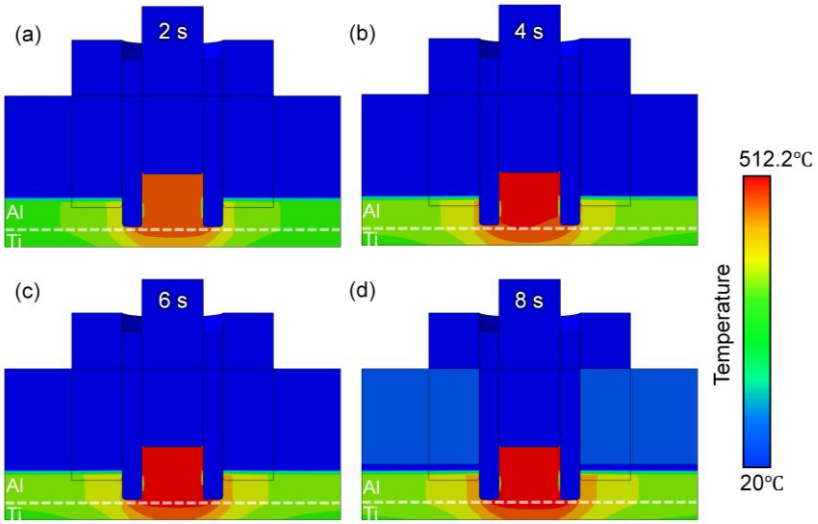


Fig. 8 The temperature field distribution: (a) 2 s; (b) 4 s; (c) 6 s; (d) 8 s.

3.2 Microstructure of the aluminum side

The temperature field distribution shows that the peak temperature of RFSSW is less than 500 ℃, which does not reach the phase-transition temperature of the Ti alloy. Therefore, only the microscopic structure of the Al side is characterized in this study. Fig. 9 (a-d) shows the morphology of joints at different dwell times, where (a1-d1) represents the microstructure of the Al side, and Fig. 9 (a2-d2), (a3-d3), and (a4-d4) are enlarged images of the stirring zone (SZ), thermo-mechanically affected zone (TMAZ), and heat-affected zone (HAZ), respectively. The joint obtained by RFSSW exhibits a superior macroscopic morphology, presenting a concentric circular shape, which can be divided into the pin stir zone (P-SZ) and sleeve stir zone (S-SZ), as well as a limited flash formation at the extrusion of the sleeve and clamping ring.

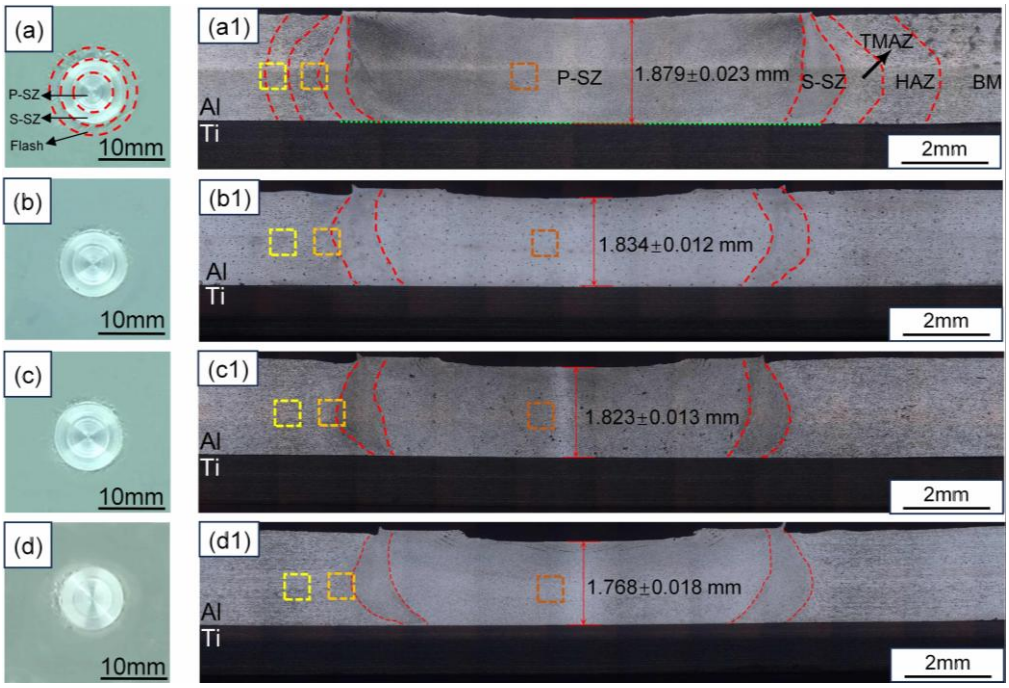


Fig. 9 The morphology of the joints: (a) 2 s; (b) 4 s; (c) 6 s; (d) 8 s.

The joint thickness exhibited a reduction from 1.879 mm to 1.768 mm with increasing dwell time. This phenomenon was attributed to extended high-temperature duration, which induced significant thermal softening of the Al substrate. The softened material experienced intensified plastic flow by tool stirring forces, leading to material expulsion and flash formation during the refilling stage. Farmanbar[26] also discovered this thinning behavior, attributing this phenomenon to thermal expansion effects. Elevated weld temperatures cause dimensional changes in both the

tool and workpiece, resulting in greater plunge depth and more material removal during the refilling process.

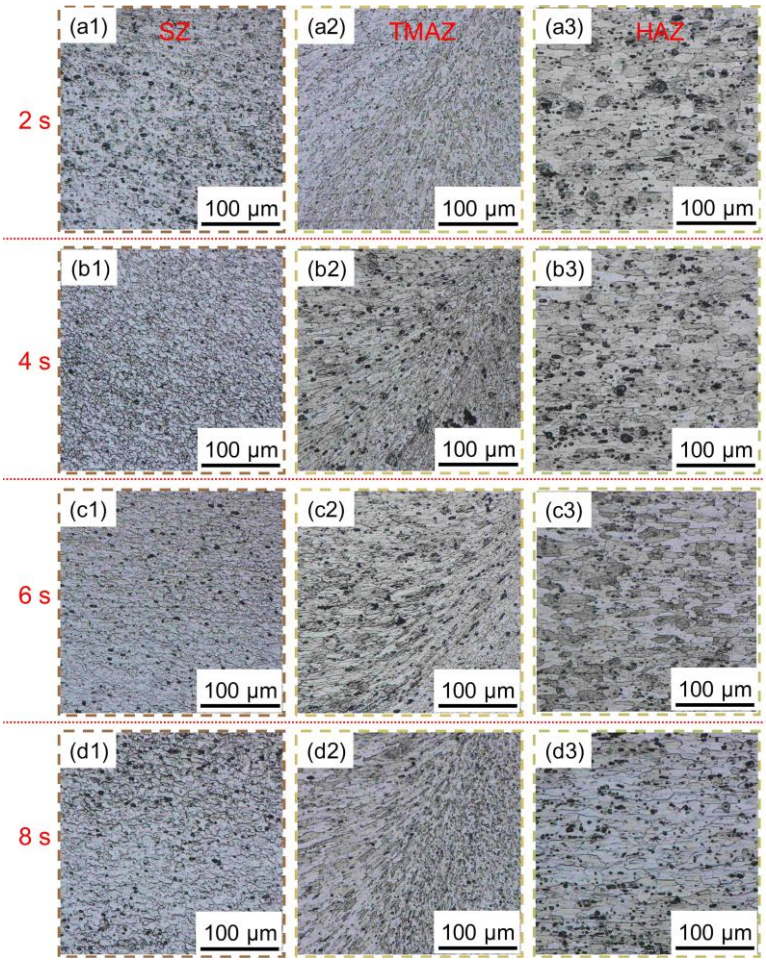


Fig. 10 The microstructure of joints: (a) 2 s; (b) 4 s; (c) 6 s; (d) 8 s.

Fig. 10 shows the microstructure of various regions of the joint at different dwell times. Within the SZ, the cooperative action of the pin and sleeve generates extreme thermomechanical conditions, subjected to maximum temperature and strain rate. This intense plastic deformation regime activates dynamic recrystallization (DRX), yielding refined equiaxed grains in SZ. Meanwhile, the SZ exhibits a concave shape due to combined axial force and radial material flow constraints. As dwell time increases from 2 s to 8 s, peak temperature gradually rises and high-temperature duration extends, thereby inducing grain size coarsening. In the TMAZ, partial grains adjacent to the SZ undergo dislocation-driven recrystallization, while other grains exhibit mechanically elongated morphologies. This microstructure arises from simultaneous exposure to thermal cycling and shear stresses, thereby forming a

distribution of refined recrystallized and deformed grains[17]. Observing the results of the strain field in Fig. 7, the shear strain during the dwelling stage is mainly concentrated around the sleeve, thus allowing the grains in this region to be mechanically elongated to form a unique TMAZ. The HAZ, located farthest from the direct-action position of the welding tool, is only subjected to thermal cycling effects. The temperature is between 341.5 ℃ and 384.1 ℃, having reached the dissolution temperature of the β" phase. In contrast to the base material (BM), the HAZ retains the as-rolled grain while exhibiting partial dissolution of precipitates.

The grain size of each region of the joint under different dwell times was analyzed using Image-Pro Plus (see Fig. 11). With increasing dwell time from 2 s to 8 s, progressive grain coarsening was observed across all joint regions. The HAZ exhibited the most significant grain growth, increasing from 35.2 μm to 45.09 μm, followed by the TMAZ (from 14.81 μm to 19.1 μm), while the SZ demonstrated the least pronounced growth (from 8.4 μm to 10.78 μm), which is attributed to the elevated thermal input originating from higher peak temperatures and extended high-temperature duration. During the dwelling stage under constant tool rotation speed, prolonged dwell time intensifies shear-driven plastic deformation within the SZ. The resulting high strain rates activate DRX mechanisms that simultaneously refine the grain structure and counteract thermal input-induced coarsening.

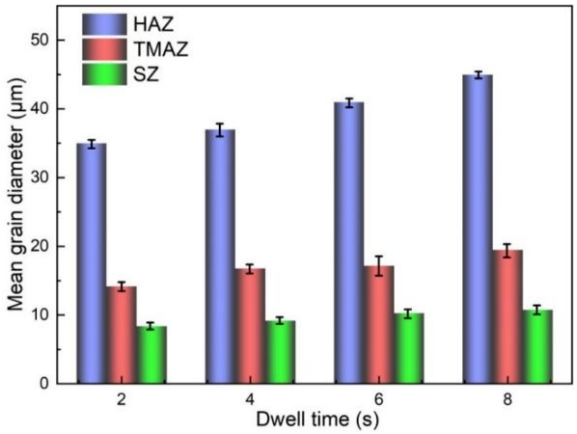


Fig. 11 The grain size of each region of the joint.

3.3 Interface characteristics and compound formation mechanism

To investigate the dwell time effects on IMCs in Al/Ti dissimilar joints, SEM

combined with line-scan EDS analysis was performed (see Fig. 12). The plunge depth was controlled at 1.8 mm (maintaining a 0.2 mm interval from the Ti substrate), producing a planar Al/Ti interface with a certain thickness diffusion layer formed via diffusion mechanism. A small number of small-sized Ti particles are brought into the Al matrix under the shearing action of plasticized material flow, as indicated by the yellow dashed lines in Fig. 12. As dwell time increases, diffusion layer thickness increases from 3.66 μm to 4.23 μm.

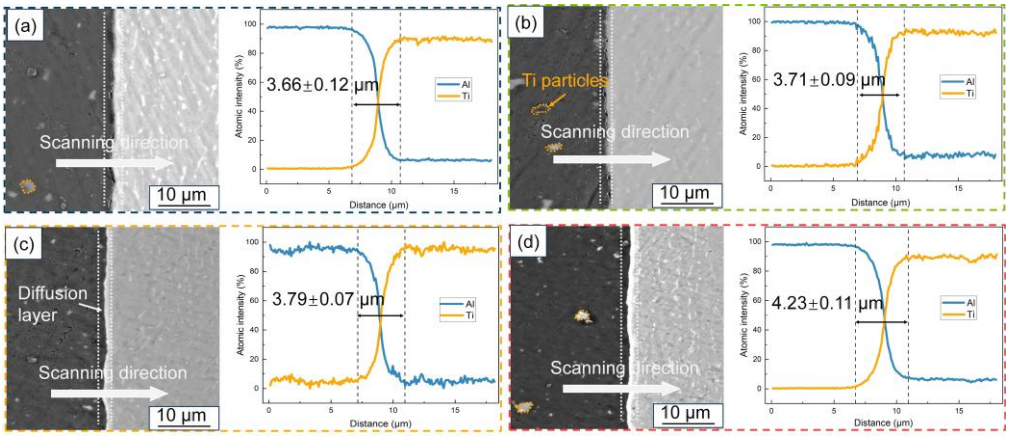


Fig. 12 The results of the line-scan with EDS: (a) 2 s; (b) 4 s; (c) 6 s; (d) 8 s.

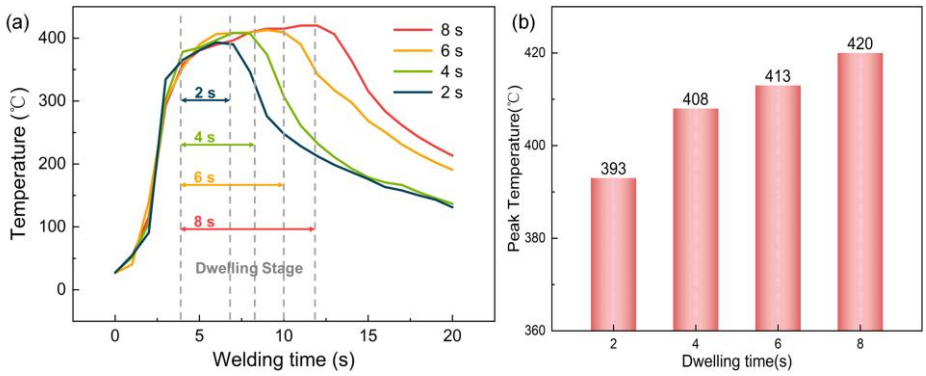


Fig. 13 Temperature measurement results at the interface: (a) thermal cycle curves under varying dwell times; (b) peak temperature variation.

According to the line scan results, no IMC layer was found at the interface. As shown in Fig. 13, as dwell time is extended from 2 s to 8 s, the peak temperature at the interface increases and can reach 393 ℃ - 420 ℃. In conventional Al/Ti solid-state diffusion bonding, temperatures exceeding 500 °C are employed, often with prolonged holding just below the melting point of the aluminum alloy to facilitate interdiffusion between Al and Ti[27]. In contrast, the RFSSW process results in approximately 400 °C at the interface and has a brief interaction time (~15 s). Despite

these milder conditions, atomic diffusion still occurred, leading to the formation of a distinct diffusion layer. This is attributed to the plastic deformation of the material induced by tool rotation, which introduces excess vacancies that promote atomic diffusion. A simplified expression for the generation rate of the excess vacancy concentration is given in Equation (5)[28]:

$$\frac{dc_{ex}(t)}{dt} = (M + T)\frac{d\epsilon}{dt} - D_v(D(t) + G)c_{ex}(t) \quad (5)$$

Where c_{ex} is the excess vacancy concentration, $\frac{d\epsilon}{dt}$ is the strain rate, D_v is the vacancy diffusion coefficient, M denotes the generation term due to dislocation motion under mechanical action, and T represents the generation term from thermally activated dislocation jog formation. The negative sign indicates contributions related to vacancy annihilation, primarily the dislocation annihilation term D and the grain boundary annihilation term G. As indicated by the strain field (see Fig. 7), the strain on the Al side reaches a maximum of 16.01 during the RFSSW process. This severe plastic deformation induces continuous generation and motion of dislocations, leading to lattice distortion that significantly elevates the excess vacancy concentration to levels orders of magnitude higher than the thermal equilibrium vacancy concentration c_{th}. According to the effective diffusion coefficient Equation (6) proposed by Militzer[29], the effective diffusion coefficient increases significantly when $\frac{c_{ex}}{c_{th}} \gg 1$. Consequently, under conditions of low temperature and high strain, diffusion occurs at the Al/Ti interface. As the processing time of the welding tool increases, the atomic diffusion distance extends, resulting in a thicker diffusion layer.

$$D^* = D_0 exp\left(-\frac{Q}{kT}\right)\left(1 + \frac{c_{ex}}{c_{th}}\right) \quad (6)$$

Where D^* is the effective diffusion coefficient, D_0 is the diffusion constant, Q is the activation energy, k is the entropy of vacancy formation and T is the temperature.

To further investigate the phase composition inside the diffusion layer, TEM was used to observe the microstructure at the interface. TEM analysis of the interfacial microstructure under optimal thermal input conditions (6 s) was conducted (Fig. 14 a). Furthermore, Fast Fourier Transform (FFT) processing was employed to analyze the selected regions within the diffusion layer, and the obtained diffraction patterns were calibrated. It can be seen from the bright-field image that a diffusion reaction occurs

at the Al/Ti interface, forming discrete IMCs, which are mainly concentrated on the Al side. The diffraction pattern obtained by FFT processing is shown in Fig. 14 (c), and after calibration, it is found to be the $TiAl_3$ phase. Meanwhile, the diffraction pattern obtained in Fig. 14 (d) was calibrated and identified as the α-Ti phase with a close-packed hexagonal structure.

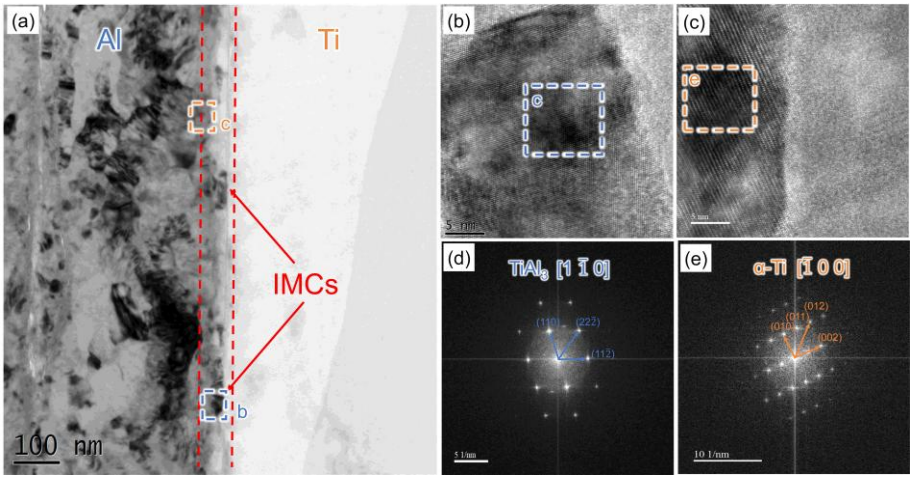


Fig. 14 TEM micrographs of the interface:(a) bright field image; (b, c) high-resolution TEM (HRTEM) images; (d, e) FFT diffraction pattern of (b) and (c).

Both SEM and TEM results reveal that the Al/Ti interface formed by RFSSW is relatively flat, suggesting that metallurgical bonding occurs through interdiffusion of atoms[30]. Although Al and Ti atoms typically form various IMCs such as Ti_3Al, TiAl, $TiAl_3$, Ti_2Al_5, $TiAl_2$ under thermal activation, only $TiAl_3$ was detected in this study. This selective formation can be rationalized based on IMC nucleation theory. The nucleation of IMCs is governed by both the Gibbs free energy of formation and the interfacial energy. Generally, IMCs with lower free energy tend to nucleate more readily. As shown in the temperature-dependent free energy curves in Fig. 15(a), within the temperature range of this study, the f free energies of TiAl and Ti_3Al are higher than that of $TiAl_3$, which explains their absence at the interface. However, $TiAl_2$, despite having the lowest free energy, was also not observed. This can be primarily attributed to the role of interfacial energy, which acts as a barrier to nucleation. The lower interfacial energy, the more favorable the nucleation of a given compound. The interfacial energies of various IMCs can be estimated using Equation

(7)[31]:

$$\gamma_{A-B} = \frac{1}{3}\left(\frac{\gamma_A+\gamma_B}{2}\right) + \frac{\Delta H_{A\ in\ B}^{interface}}{C_0 V_A^{2/3}} \quad (7)$$

Where $\Delta H_{A\ in\ B}^{interface}$ is the enthalpy change upon solution of 1 mole of A in an infinitely large reservoir of B; V_A is the molar volume of atom; C_A and C_B are the atom concentration; γ_A is the surface energy (γ_{Al}=200 mJ/m^2, γ_{Ti}=2050 mJ/m^2). The calculated interfacial energy for $TiAl_3$ and $TiAl_2$ are 450 mJ/m^2 and 480 mJ/m^2, respectively. Consequently, $TiAl_3$ nucleates preferentially at the interface and continues to grow under diffusion-controlled mechanisms.

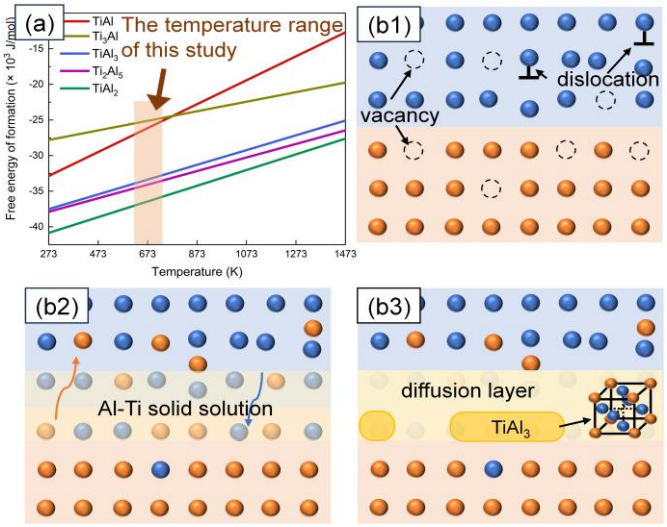


Fig. 15 Diffusion mechanism at the interface: (a) the temperature-dependent Gibbs free energy of formation curves; (b) the schematic illustration of the diffusion layer formation mechanism.

From the above analysis, a diffusion layer is formed at the RFSSW interface, within which $TiAl_3$ is discretely distributed rather than forming a continuous IMC layer. According to IMC growth kinetics, the thickness of the IMC layer depends on both time and kinetic constants, as expressed in Equations (8) and (9):

$$x = k(t - t_0)^n \quad (8)$$

$$k = k_0 exp\left(\frac{-Q_k}{RT}\right) \quad (9)$$

Where x is the thickness of the IMC layer; k is the growth kinetics constant; t is time; n is the growth kinetics exponent; k_0 is the pre-exponential factor; Q_k is the growth activation energy for $TiAl_3$; R is the gas constant (8.31 J/(mol·K)). Owing to the brief thermal cycle experienced at the interface during RFSSW, $TiAl_3$ remains in

the chemical reaction stage within a few seconds and does not have sufficient time to grow. Consequently, nucleation occurs only at energetically favorable sites, resulting in the formation of discrete IMCs. The schematic illustration of the diffusion layer formation mechanism at the Al/Ti interface is presented in the Fig. 15(b). The presence of abundant crystal defects, such as vacancies and dislocations, facilitates the interdiffusion of Al and Ti atoms, leading to the formation of an Al–Ti solid solution layer. With increasing temperature and time, the solid solution becomes supersaturated, promoting the development of a diffusion layer of obvious thickness. Within this layer, $TiAl_3$ nucleates preferentially. Owing to the short duration of the RFSSW process, the IMCs exhibit a discrete, sheet-like morphology distributed along the interface.

3.4 Mechanical properties and fracture mechanism

Fig. 16 (a) presents the transverse Vickers microhardness profiles across joint regions under varying dwell times. As dwell time increases from 2 s to 8 s, the overall hardness values decrease, attributable to extended high-temperature duration, which facilitates grain coarsening, thereby diminishing the grain refinement strengthening efficacy. Microhardness analysis at the same dwell time reveals superior hardness in the BM compared to the weld region. This behavior originates from the reduced density of precipitated phases during welding thermal cycles, which weakens the precipitation strengthening mechanism in 6061 alloy[10]. The SZ, TMAZ, and HAZ undergo varying degrees of precipitate dissolution, whereas the BM retains a high-density distribution of metastable β" precipitates, thereby sustaining enhanced microhardness through Orowan strengthening mechanisms. The TMAZ exhibits the lowest microhardness due to two factors. First, unlike the SZ, which undergoes adequate DRX and grain refinement, the TMAZ experiences incomplete recrystallization, resulting in limited grain refinement and diminished fine-grain strengthening. Additionally, the SZ benefits from natural aging-induced reprecipitation, promoting precipitation strengthening. Secondly, compared to the HAZ, the TMAZ's proximity to the welding heat source accelerates the coarsening and dissolution of precipitates. This dual deterioration of both grain-boundary and

precipitation strengthening mechanisms collectively positions the TMAZ as the region of minimal hardness. The SZ generally exhibits higher microhardness than the HAZ due to its refined grain structure and precipitation. However, at the dwell time of 8 s, excessive heat input triggers pronounced grain coarsening in the SZ, reducing its hardness below that of the HAZ. The vertical hardness profile (see Fig. 16b) reveals a steep gradient across the SZ centerline, transitioning from the Al alloy to the Ti alloy. This abrupt hardness shift is primarily attributed to the intrinsic hardness contrast between the Al and Ti.

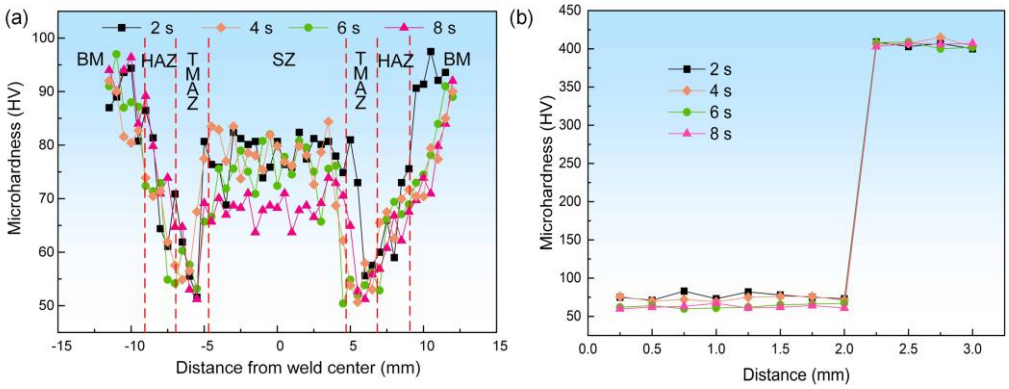


Fig. 16 The Vickers microhardness: (a) transverse; (b) vertical.

Fig. 17 presents macrostructural characteristics of tensile-shear fracture surfaces in spot-welded joints corresponding to varying dwell times. The fracture analysis reveals that the failure characteristics in Al/Ti RFSSW joints are predominantly interface failure. The failure load and adhesion area of Al at the Ti side were statistically analyzed, as shown in Fig. 17 (e). As the dwell time increases, the tensile strength exhibits an initial increase followed by a decrease. Peak performance emerges at 6 s, achieving maximum load (6.39 kN) through optimized interfacial bonding. With increasing dwell time from 2 s to 6 s, the prolonged high-temperature duration and cumulative thermal input to the joint continuously facilitate atomic interdiffusion at Al/Ti interfaces. Accordingly, with prolonged dwell time under the thermomechanical coupling effect, the interfacial metallurgical bonding quality improves gradually, leading to an expansion of the effective joint connection area and a concomitant enhancement in tensile strength. However, when extending to 8 s, despite achieving maximum bonding area, the tensile-shear failure load of the joint

decreased. This strength degradation originates from grain coarsening in the lower Al substrate region due to excessive thermal input. The elevated thermal input accelerates elemental diffusion at the Al/Ti interface, which promotes the formation of a thicker diffusion layer. As shown in Fig. 17 (f-g), the coarse grain zone at the interface also expands correspondingly, diminishing the grain refinement strengthening effect[30].

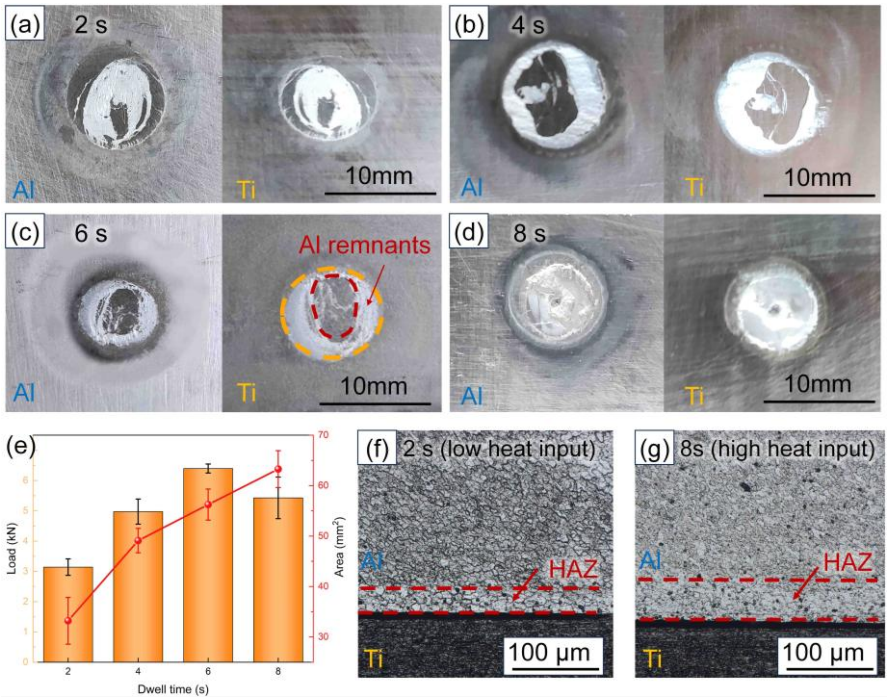


Fig. 17 Fracture characteristics: (a-d) tensile-shear fracture surfaces; (e) the failure load and the bonding area of Al remnants; (f-g) the coarse grain zone at the interface.

The fracture morphology of the Al side is shown in the Fig. 18 (a). The outer ring is S-SZ with a rough surface, while the inner ring is P-SZ with a smoother surface. SEM examination of the S-SZ shows a distribution of ductile dimples, indicative of significant plastic deformation. In contrast, the P-SZ exhibits a flat fracture surface characteristic of brittle failure, along with numerous dispersed particles. EDS analysis suggests that these are likely Ti particles and $TiAl_3$, as presented in Table 4. Owing to the varying thermomechanical conditions experienced by the Al sheet, the fracture exhibits a mixed mode. The schematic of the fracture mechanism is illustrated in the Fig. 18 (e). On the Al side, coarse grain zone is present near the interface, along with Ti particles introduced by plastic flow. Additionally, discrete sheet-like $TiAl_3$ is

observed at the interface. Under tensile-shear loading, cracks initiate around hard particles and propagate along coarse grain zone, ultimately leading to complete joint failure. Prolonged tool dwelling results in severe grain coarsening in the S-SZ, promoting fracture through this coarsened zone, accompanied by aluminum adhesion. Meanwhile, the dispersed Ti particles and $TiAl_3$ at the interface facilitate crack propagation, leading to direct interfacial fracture.

Table 4 EDS results of fracture surface.

	Element content (at.%)		Phase
	Al	Ti	
1	7.14	92.86	Ti
2	74.88	25.12	$TiAl_3$

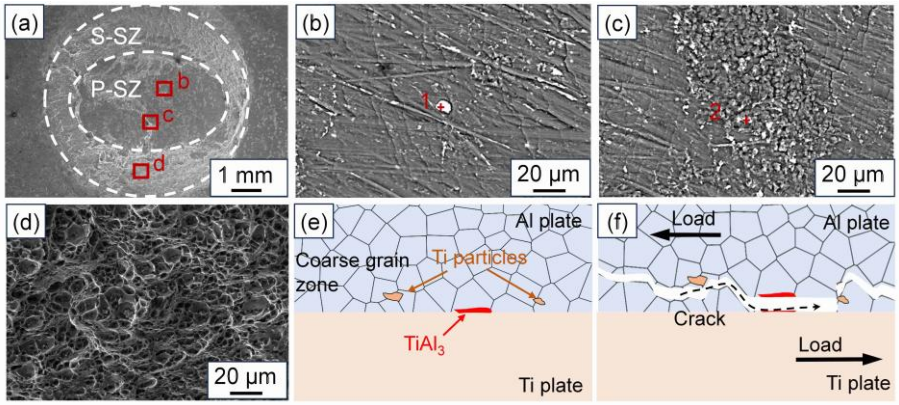


Fig. 18 Fracture behavior of Al/Ti joints: (a) tensile-shear fracture morphology; (b-c) the high magnification image of P-SZ; (d) the high magnification image of S-SZ; (e-f) the schematic of the fracture mechanism.

4 Conclusion

The microstructure and mechanical properties of the Al-Ti joints by refill friction stir spot welding were investigated, and the main conclusions are as follows:

(1) The numerical simulations demonstrate the capability of RFSSW to produce defect-free joints. Strain field analysis reveals a gradual intensification of strain localization at the end of the sleeve periphery, accompanied by asymmetric strain distribution between the AS and RS, with higher strain concentration on the AS due to thermomechanical effects. Additionally, prolonged dwell time from 2 to 8 s gradually elevates the peak temperature from 393 ℃ to 420 ℃ while extending the high-temperature duration.

(2) As the dwell time increased, the weld thickness progressively decreased from 1.879 mm to 1.768 mm, an effect attributed to material softening. The SZ features refined equiaxed grains through DRX. Prolonged dwell time induces SZ grain size increases from 8.4 to 10.78 μm. Meanwhile, the interfacial diffusion layer thickens from 3.66 to 4.23 μm, concurrent with thermally activated IMCs formation. TEM analysis reveals that the IMCs at the interface are mainly composed of $TiAl_3$ and α-Ti phases.

(3) The preferential nucleation and exclusive formation of $TiAl_3$ are attributed to its minimal Gibbs free energy and interfacial energy. Despite the low temperature (~400 ℃) and short duration (~15 s) of the process, atomic interdiffusion was enabled by the abundance of vacancies and dislocations introduced through plastic deformation. However, the short duration limited growth, resulting in a discontinuous $TiAl_3$ layer at the interface.

(4) The joint hardness demonstrates an inverse correlation with dwell times, primarily attributed to grain coarsening. The TMAZ displayed the lowest hardness, due to both grain coarsening and the dissolution of precipitates. The tensile-shear failure load peaked at 6.39 kN at 6 s before decreasing. The failure characteristics in Al/Ti RFSSW joints are interface failure, characterized by crack initiation at hard particles within the Al side and subsequent propagation along both the coarse grain zone and the discontinuous $TiAl_3$ layer at the interface.

References

[1] Zhao JT, Xu B, Jiang P, Song MJ, Geng SN (2024) Innovative insight for microstructural regulation of intermetallic compounds in Ti/Al dissimilar alloy laser welding: micro-surface texturing via pulsed laser pretreatment. J Manuf Process 132:824-836. https://doi.org/10.1016/j.jmapro.2024.10.052

[2] Bang KS, Lee KJ, Bang HS, Bang HS (2011) Interfacial microstructure and mechanical properties of dissimilar friction stir welds between 6061-T6 aluminum and Ti-6%Al-4%V alloys. Mater Trans 52(5):974-978.

https://doi.org/10.2320/matertrans.L-MZ201114

[3] Tian RY, Chen S, Yang BY, Wu JW, Li P, Chen NN, Li HY, Wang Q, Xia HB, Ma NS (2023) Elemental diffusion, atomic substitution mechanisms and interfacial fracture behavior in laser welded–brazed Al/Ti. Mater Charact 202:112998. https://doi.org/10.1016/j.matchar.2023.112998

[4] Cho D, Ghassemi-Armaki H, Stoughton TB, Carlson BE, Sung HM, Hwang J, Legarth BN, Yoon JW (2024) Fracture mechanisms of Al-steel resistance spot welds: the role of intermetallic compound phases. Eng Fract Mech 311:110520. https://doi.org/10.1016/j.engfracmech.2024.110520

[5] Johannes AÖ, Christian P, Georg K, Weinberger T, Schlögl CM, Suppan W, Radlmayr KM (2024) Dissimilar friction stir welding and post-weld heat treatment of Ti-6Al-4V and AA7075 producing joints of unprecedented strength. J Adv Join Process 9:100213. https://doi.org/10.1016/j.jajp.2024.100213

[6] Sen M, Puri AB (2022) Formation of intermetallic compounds (IMCs) in FSW of aluminum and magnesium alloys (Al/Mg alloys) − a review. Mater Today Commun 33:105017. https://doi.org/10.1016/j.mtcomm.2022.105017

[7] Zhou L, Yu M, Zhao H, Jiang ZH, Guo F, Song XG (2019) Dissimilar friction stir welding of AA6061 and Ti6Al4V alloys: a study on microstructure and mechanical properties. J Manuf Process **48**:119-126. https://doi.org/10.1016/j.jmapro.2019.09.043

[8] Zhang Z, Zhang XY, Liu YL, Xing HN (2025) The interface reaction and microstructure control in friction stir lap welding of Al and Ti dissimilar alloys. J Mater Res Technol 35:6700-6714. https://doi.org/10.1016/j.jmrt.2025.03.012

[9] Fu BL, Shen JJ, Suhuddin UFH, Pereira AAC, Maawad E, Santos JF, Klusemann B, Rethmeier M (2021) Revealing joining mechanism in refill friction stir spot welding of AZ31 magnesium alloy to galvanized DP600 steel. Mater Design 209:109997. https://doi.org/10.1016/j.matdes.2021.109997

[10] Shen Z, Li WY, Ding Y, Hou W, Liu XC, Guo W, Chen HY, Liu X, Yang J, Gerlich AP (2020) Material flow during refill friction stir spot welded dissimilar Al alloys using a grooved tool. J Manuf Process 49:260-270.

https://doi.org/10.1016/j.jmapro.2019.11.029

[11] Zhao YQ, Dong CL, Wang CG, Miao S, Tan JH, Yi YY (2020) Microstructures evolution in refill friction stir spot welding of Al-Zn-Mg-Cu alloy. Metals-Basel 10(1):145. https://doi.org/10.3390/met10010145

[12] Feng XS, Li SB, Tang LN, Wang HM (2020) Refill friction stir spot welding of similar and dissimilar alloys: a review. Acta Metall Sin 33:30-42. https://doi.org/10.1007/s40195-019-00982-4

[13] Vacchi GS, Silva R, Plaine AH, Suhuddin UFH, Alcântara NG, Sordi VL, Rovere CAD (2020) Refill friction stir spot welded AA5754-H22/Ti-6Al-4V joints: microstructural characterization and electrochemical corrosion behavior of aluminum surfaces. Mater Today Commun 22:100759. https://doi.org/10.1016/j.mtcomm.2019.100759

[14] Li YX, Sun GD, Zhang ZL, Zhou L, Guo N, Meng Q, Dong JH, Zhao HX (2023) Texture evolution of refill friction stir spot welding in alclad 2A12-T42 aluminum alloy. Mater Charact 205:113289. https://doi.org/10.1016/j.matchar.2023.113289

[15] Yuan YF, Wu ZX, Chen KL, Liu HH, Huang H, Li YB (2025) Effects of plunge depth on macro-/microstructure and mechanical properties of refill friction stir spot welded 2195-T6 Al-Li alloy. J Mater Res Technol 35:6026-6041. https://doi.org/10.1016/j.jmrt.2025.02.046

[16] Ferrari VR, Coury FG, Suhuddin UFH, Alcântara NG, Santos JF, Ohashi R, Fujimoto M, Koga GY (2022) Effects of semi-solid structure on interface formation of dissimilar aluminum to galvanized steel welds produced by load-controlled refill friction stir spot welding. J Manuf Process 84:298-315. https://doi.org/10.1016/j.jmapro.2022.10.001

[17] Yu MR, Zhao HY, Zhang ZL, Zhou L, Song XG (2022) Friction surfacing assisted refilled friction stir spot welding of AA6061 alloy and Q235 steel. J Manuf Process 77:1-12. https://doi.org/10.1016/j.jmapro.2022.03.006

[18] Zou YF, Li WY, Yang XW, Su Y, Chu Q, Shen ZK (2022) Microstructure and mechanical properties of refill friction stir spot welded joints: effects of tool size

and welding parameters. J Mater Res Technol 21:5066-5080. https://doi.org/10.1016/j.jmrt.2022.11.108

[19] Chen CB, Guo T, Zhao YQ, Zhang K (2026) Numerical simulation of friction stir welding of dissimilar 6061/7050 aluminum alloys. J Plasticity Eng 33(6):131-142.

[20] Amir R. Ali ZB, Alireza Z, Hamed DA (2026) Numerical and experimental investigation of cutting force in rotary broaching process of Ti6Al4V using Johnson–Cook constitutive model. J Eng Res. https://doi.org/10.1016/j.jer.2026.04.034

[21] Zhang XK, Shi L, Wu CS, Yang CL, Gao S (2023) Multi-phase modelling of heat and mass transfer during Ti/Al dissimilar friction stir welding process. J Manuf Process 94:240-254. https://doi.org/10.1016/j.jmapro.2023.03.037

[22] Nan XC, Zhao HY, Ma CY, Sun SL, Sun GD, Xu ZY, Zhou L, Wang R, Song XG (2023) Interface characterization and formation mechanism of Al/Ti dissimilar joints of refill friction stir spot welding. Int J Adv Manuf Technol 126:1539–1551. https://doi.org/10.1007/s00170-023-11226-2

[23] Iftikhar SH, Cherupurakal N, Krishnapriya R, Mourad AHI (2024) Friction stir spot welding of recycled scrap thermoplastics. Int J Lightweight Mater Manuf 7(6):838-848. https://doi.org/10.1016/j.ijlmm.2024.06.003

[24] Janga VSR, Awang M, Sallih N, Lemma TA (2025) Thermo-mechanical and material flow characteristics of tool sequencing dynamics in refill FSSW of thin alclad AA7075-T6 sheets: numerical analysis using meshless smoothed-particle hydrodynamics method. J Adv Join Process 11:100285. https://doi.org/10.1016/j.jajp.2025.100285

[25] Xue W, Xiao LY, Huang CQ, He DQ, Ren XQ (2024) Asymmetric study on the microstructure and mechanical properties of friction stir welded joints: finite element simulation and experiment. CIRP J Manuf Sci Tec 55:108-128. https://doi.org/10.1016/j.cirpj.2024.09.006

[26] Farmanbar N, Mousavizade SM, Ezatpour HR (2019) Achieving special mechanical properties with considering dwell time of AA5052 Sheets welded by

a simple novel friction stir spot welding. Mar Struct 65:197-214. https://doi.org/10.1016/j.marstruc.2019.01.010

[27] Thiyaneshwaran N, Sivaprasad K, Ravisankar B (2021) Characterization based analysis on $TiAl_3$ intermetallic phase layer growth phenomenon and kinetics in diffusion bonded Ti/$TiAl_3$/Al laminates. Mater Charact 174:110981. https://doi.org/10.1016/j.matchar.2021.110981

[28] Vullum PE, Celotto A, Grong Ø, Holmestad R (2025) Cold bonding of aluminum to copper by deformation-enhanced diffusion. Sci Rep 15:41656. https://doi.org/10.1038/s41598-025-25620-1

[29] Militzer M, Sun WP, Jonas JJ (1994) Modelling the effect of deformation-induced vacancies on segregation and precipitation. Acta Metall Mater 42(1):133-141. https://doi.org/10.1016/0956-7151(94)90056-6

[30] Zuo YY, Gao YS, Liu HJ, Huang YX (2025) Enhanced strength of Al/Ti dissimilar joints via trailing support friction stir welding at high welding velocities. Mater Charact 225:115174. https://doi.org/10.1016/j.matchar.2025.115174

[31] Liu JP, Su YQ, Xu YJ, Luo LS, Guo JJ, Fu HZ (2011) First phase selection in solid Ti/Al diffusion couple. Rare Metal Mat Eng 40(5):753-756. https://doi.org/10.1016/S1875-5372(11)60031-3

Acknowledgements

The research was supported by the National Natural Science Foundation of China (No. 52375316).

Author information

Authors and Affiliations

State Key Laboratory of Precision Welding & Joining of Materials and Structures, Harbin Institute of Technology, Harbin, 150001, People's Republic of China

Jiancheng Wang, Li Zhou, Xinchen Nan, Shikang Gao, Yuchun Liu & Xiaoguo Song

Shandong Provincial Key Laboratory of Special Welding Technology, Harbin

Institute of Technology at Weihai, Weihai 264209, People's Republic of China

Jiancheng Wang, Li Zhou, Xinchen Nan, Chengyue Ma, Shikang Gao, Yuchun Liu & Xiaoguo Song

Contributions

Jiancheng Wang: Writing-original draft, Conceptualization, Formal analysis, Investigation, Software, Validation. Li Zhou: Writing-review and editing, Funding acquisition, Methodology, Conceptualization. Xinchen Nan: Formal analysis; Investigation, Software, Validation. Chengyue Ma: Methodology, Project Administration, Validation, Visualization. Shikang Gao: Writing-review and editing, Methodology, Investigation, Supervision. Yuchun Liu: Software, Validation, Writing-review and editing. Xiaoguo Song: Writing-review and editing, Supervision.

Corresponding authors

Correspondence to Shikang Gao or Li Zhou.

Ethics declarations

Conflict of interest

On behalf of all authors, the corresponding author states that there is no conflict of interest.